Earth and Planetary Science Letters 413 (2015) 13–24

Contents lists available at ScienceDirect

Earth and Planetary Science Letters

www.elsevier.com/locate/epsl

Tearing of the Indian lithospheric slab beneath southern Tibet revealed by SKS-wave splitting measurements

Yun Chen [a,*], Wei Li [a,b], Xiaohui Yuan [c], José Badal [d], Jiwen Teng [a]

[a] State Key Laboratory of Lithospheric Evolution, Institute of Geology and Geophysics, Chinese Academy of Sciences, Beijing 100029, China
[b] University of Chinese Academy of Sciences, Beijing 100049, China
[c] Deutsches GeoForschungsZentrum GFZ, Telegrafenberg, 14473 Potsdam, Germany
[d] Physics of the Earth, Sciences B, University of Zaragoza, Pedro Cerbuna 12, 50009 Zaragoza, Spain

ARTICLE INFO

Article history:
Received 3 September 2014
Received in revised form 16 December 2014
Accepted 22 December 2014
Available online xxxx
Editor: A. Yin

Keywords:
seismic anisotropy
shear wave splitting
subducting lithospheric slab
slab tearing
Himalayan–Tibetan collision zone

ABSTRACT

Shear wave birefringence is a direct diagnostic of seismic anisotropy. It is often used to infer the northern limit of the underthrusting Indian lithosphere, based on the seismic anisotropy contrast between the Indian and Eurasian plates. Most studies have been made through several near north–south trending passive-source seismic experiments in southern Tibet. To investigate the geometry and the nature of the underthrusting Indian lithosphere, an east–west trending seismic array consisting of 48 seismographs was operated in the central Lhasa block from September 2009 to November 2010. Splitting of SKS waves was measured and verified with different methods. Along the profile, the direction of fast wave polarization is about 60° in average with small fluctuations. The delay time generally increases from east to west between 0.2 s and 1.0 s, and its variation correlates spatially with north–south oriented rifts in southern Tibet. The SKS wave arrives 1.0–2.0 s later at stations in the eastern part of the profile than in the west. The source of the anisotropy, estimated by non-overlapped parts of the Fresnel zones at stations with different splitting parameters, is concentrated above ca. 195 km depth. All the first-order features suggest that the geometry of the underthrusting Indian lithospheric slab in the Himalayan–Tibetan collision zone beneath southern Tibet is characterized by systematic lateral variations. A slab tearing and/or breakoff model of Indian lithosphere with different subduction angles is likely a good candidate to explain the observations.

1. Introduction

Mountain belts created by continent–continent collisions are perhaps the most dominant geologic features of the surface on Earth. The most spectacular one of them is the Himalayan–Tibetan orogen, consisting of the east–west trending high-altitude Himalaya and Karakorum ranges in the south and the vast Tibetan Plateau in the north (e.g., Dewey and Burke, 1973; Yin and Harrison, 2000). This orogenic system was largely created by the Indo-Asian collision over the past 50 Ma with an east–west extent of more than 2000 km from the Nanga Parbat syntaxis in the west to the Namche Barwa syntaxis in the east (Fig. 1). It is part of the greater Tethyan orogenic belt that extends from the Mediterranean Sea to the Sumatra arc over a distance of more than 7000 km (Yin and Harrison, 2000).

Plate motion and deformation can create distinct pattern in seismic anisotropy in the lithosphere and asthenosphere. Shear wave birefringence is viewed as a direct diagnostic of seismic anisotropy. Core-related phases (e.g., SKS, PKS or SmKS) are commonly used to investigate the continental anisotropy (Silver and Chan, 1991; Savage, 1999). As P-to-S converted waves at the core-mantle boundary (CMB), they should be purely SV polarized in an isotropic Earth with a linear particle motion in the radial direction. If a SKS wave propagates in an anisotropic region between the CMB and the receiver, it will split into two orthogonal waves with polarization in the fast and slow directions, respectively (Alsina and Snieder, 1995). The two waves arrive at a station with a time lag, resulting in birefringence and elliptic particle motion. Analyzing SKS splitting can provide detailed information of azimuthal anisotropy, defined by the fast speed direction and delay time. One advantage of the SKS phase is the good lateral resolution due to near-vertical incidence.

Over the last two decades several large-scale seismic experiments have been carried out in Tibet, including the 1991–1992 PASSCAL (McNamara and Owens, 1994), INDEPTH

* Corresponding author. Tel.: +86 10 8299 8339; fax: +86 10 8299 8001.
E-mail address: yunchen@mail.iggcas.ac.cn (Y. Chen).

http://dx.doi.org/10.1016/j.epsl.2014.12.041
0012-821X/

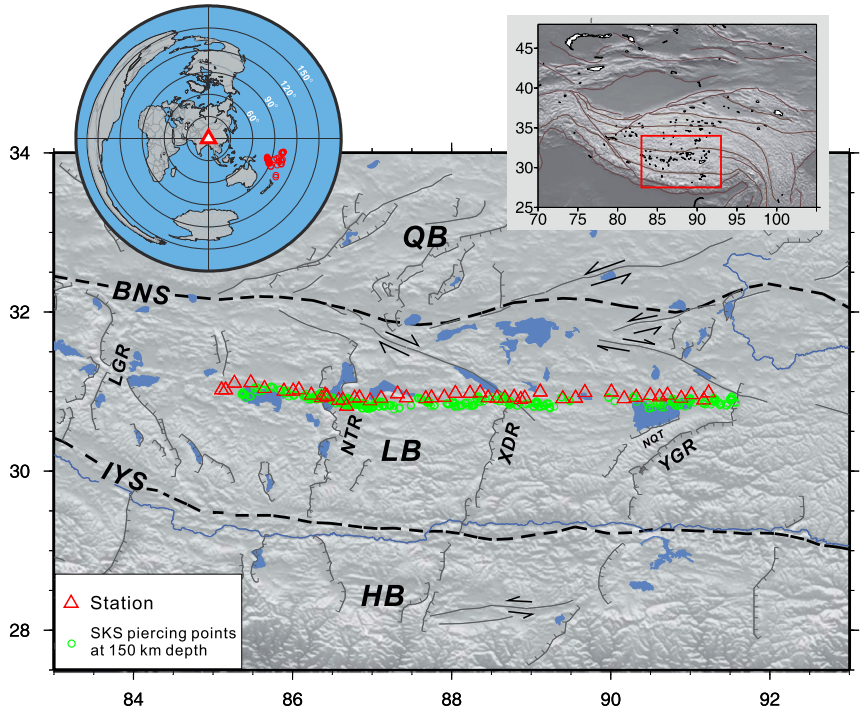

Fig. 1. Shaded topographic map showing the regional geologic features in southern Tibet and the location of the TIBET-31N seismic array. Geological structures are based on the HimaTibetMap-1.0 dataset (Styron et al., 2010). Red triangles indicate seismic stations. Green dots denote SKS-wave piercing points at 150-km depth. Blue areas are lakes. The upper-right inset is a map of the Tibetan Plateau where the study area is delimited by a red rectangle. The upper-left inset is the map showing the distribution of earthquakes used for the SKS-wave spitting measurements. The red triangle denotes the approximate location of the seismic array. The 42 events used for the SKS splitting analysis are represented as red circles, and they all lie in the Fiji–Tonga–Kermadec region with similar backazimuths and ray parameters. Abbreviations for tectonic blocks: HB, Himalayan block; LB, Lhasa block; QB, Qiangtang block. Abbreviations for sutures: IYS, Indus–Yarlung suture; BNS, Bangong–Nujiang suture. Abbreviations for rifts: LGR, Longgar rift; NTR, Nyima–Tingri rift; XDR, Xainza–Dingjye rift; YGR, Yadong–Gulu rift. NQT: Nyainqentanglha Mountains.

(Sandvol and Ni, 1997; Huang et al., 2000), Hi-CLIMB (Nabelek et al., 2009), ANTILOPE (Zhao et al., 2010, 2013, 2014), etc. Most of the seismic arrays are mainly north–south trending. Undoubtedly the N–S trending transects are optimal to investigate the contacts among different blocks and the deep dynamic process of the N–S convergence between India and Eurasia. Shear wave splitting was used to measure the seismic anisotropy and to infer the frontiers of the northwards moving Indian plate. Sandvol and Ni (1997) analyzed the shear wave splitting of the INDEPTH-II seismic array. Their results show no evidence of significant seismic anisotropy in Lhasa block. Chen and Özalaybey (1998) modeled seismic anisotropy and Bouguer gravity anomalies along the profile from Yadong to Golmud (1991–1992 PASSCAL) by a juxtaposition of the Eurasian lithosphere over Indian lithosphere. The Eurasian mantle lithosphere appears only to north of 30°N, while the Indian mantle lithosphere extends farther north to near 33°N. Huang et al. (2000) suggested that the onset of measurable splitting at 32°N from the INDEPTH III seismic array most likely marks the northern limit of the underthrusting Indian lithosphere. Fu et al. (2008) combined the shear wave splitting results in Tibet and interpreted the nulls near the Indus–Yarlung suture as a result of a corner flow induced by the subvertical subduction of the Indian lithosphere south of the Bangong–Nujiang suture. Similarly, Zhao et al. (2010) measured the SKS anisotropy along the ANTILOPE-I and II profiles and defined the scope of the Indian lithosphere by the feature of weak anisotropy. Chen et al. (2010a) combined SKS splittings along the Hi-CLIMB profile with other observations, such as *He* isotopes and gravity observations, and argued that the rapid increase in the splitting magnitude occurring about 100 km north of the Bangong–Nujiang suture reflects the northern leading edge of the underthrusting Indian mantle lithosphere. Kind and Yuan (2010) presented a comprehensive map of the northern boundary of the Indian lithosphere at 200 km depth inferred from tomography, receiver function and seismic anisotropy measurements. A point of agreement from most previous studies is that the Indian mantle lithosphere advancing northward and subducting beneath Tibet is accompanied by no or very weak anisotropy (Meissner et al., 2002; Kumar and Singh, 2008). Therefore the transition from null and weak shear wave splitting to strong splitting may indicate the leading edge of the northwards underthrusting Indian lithosphere (Hirn et al., 1995).

Supplementary to the N–S trending seismic experiments, east–west trending experiments in southern Tibet could help to trace lateral variations in the geometry and the nature of the underthrusting Indian lithosphere. The Lhasa block, located between the Bangong–Nujiang suture to the north and the Indus–Yarlung suture to the south (Fig. 1), is an ideal place to investigate the lateral variations of the underthrusting Indian lithosphere. A 600-km-long east–west passive-source linear seismic array (TIBET-31N) was operated approximately along 31°N latitude from Nam Tso to Cuoqin in the central Lhasa block, crossing some north–south oriented major rift-systems (or grabens) in southern Tibet (Fig. 1). In this experiment, 48 seismographs (equipped with Guralp CMG-3ESP sensors plus Reftek-72A or Reftek-130 data loggers) were operated from September 2009 to November 2010 at an average station spacing of 15 km along with a co-operating profile of 10 seismographs across Yadong–Gulu Rift (Zhang et al., 2013).

2. Data and methods

In this study, we used shear-wave splitting analysis to detect azimuthal anisotropy beneath the profile TIBET-31N. In order to identify the most salient first-order features of our splitting data

Table 1
Events used for SKS splitting analysis in this study.

Year	Julian day	UTC time (hhmmss)	Latitude (deg.)	Longitude (deg.)	Mag. (Mw)	Depth (km)
2009	272	174810	−15.49	−172.10	8.1	18
2009	275	010739	−16.33	−173.47	6.1	8
2009	275	154709	−17.02	174.51	6.0	10
2009	281	211613	−12.91	166.31	5.9	35
2009	282	131232	−13.36	166.50	5.6	35
2009	283	142515	−14.12	166.69	5.8	35
2009	284	031213	−22.00	170.25	6.0	10
2009	284	044751	−13.00	166.12	5.7	44
2009	285	205938	−14.07	166.25	5.7	35
2009	287	180021	−14.91	−174.82	6.2	10
2009	292	224938	−15.36	−172.26	5.9	18
2009	296	151413	−12.20	166.05	5.9	31
2009	304	190951	−11.38	166.38	5.9	133
2009	306	104713	−24.12	−175.17	6.1	9
2009	312	154609	−16.01	167.99	5.5	179
2009	313	104454	−17.24	178.34	7.3	585
2009	326	074820	−17.79	−178.43	6.3	522
2009	326	224727	−31.57	179.47	6.2	435
2009	327	183634	−12.62	166.25	5.7	35
2009	328	124715	−20.71	−174.04	6.7	18
2009	335	194258	−17.08	167.64	5.5	40
2009	343	094603	−22.15	170.96	6.4	45
2010	018	160914	−12.48	166.29	5.7	10
2010	024	181509	−18.51	167.90	5.6	15
2010	040	010344	−15.05	−173.49	6.0	10
2010	044	023428	−21.90	−174.77	6.0	11
2010	053	070052	−23.64	−176.04	5.9	25
2010	063	140227	−13.57	167.23	6.4	176
2010	100	165424	−20.11	−176.22	5.9	272
2010	101	021906	−12.97	166.52	5.8	10
2010	111	172029	−15.27	−173.22	6.1	35
2010	147	171446	−13.70	166.64	7.1	31
2010	152	164732	−17.88	169.10	5.6	40
2010	153	185107	−13.73	166.59	5.6	35
2010	160	232317	−18.60	169.49	6.0	12
2010	168	130646	−33.17	179.72	6.0	170
2010	181	043102	−23.31	179.12	6.3	581
2010	183	060403	−13.64	166.49	6.3	29
2010	203	050357	−15.15	168.17	5.9	10
2010	222	052344	−17.54	168.07	7.2	25
2010	222	231831	−14.46	167.35	5.9	191
2010	228	193549	−20.80	−178.83	6.1	603

set and hence to infer the physical meanings by a simple pattern, the following strategies and approaches were adopted.

(1) Only SKS phases with high signal-to-noise ratio on the original trace were selected for analysis. To avoid complications and to ensure a high lateral resolution, other phases (e.g., SKKS waves) were not considered, because SKS phase has a steeper incidence at the receiver and a clearer arrival than other shear-wave phases for the same event (see Fig. 2a in Chen et al., 2013).

(2) We selected events located in the Fiji–Tonga subduction zone with similar backazimuths and ray parameters (Table 1). So, complicated propagating effects that might affect our measurements, such as a large spatial sampling difference of different ray paths, and superposition of unequal anisotropic properties from different azimuths, are minimized. On the whole, 42 events are used for the SKS splitting analysis (Fig. 1). Locations of the SKS piercing points at a depth of 150 km beneath the stations are shown in Fig. 1. They are distributed within a narrow band close to the profile.

(3) To enhance the signal-to-noise ratio, the records were band-pass filtered by two filters: a high-pass filter with a corner frequency of 0.02 Hz to suppress the long-period noise, and a low-pass filter with a corner frequency between 0.2 and 1.0 Hz to remove the high-frequency scattering induced by small-scale heterogeneities.

(4) Different analyzing methods for shear wave splitting were used simultaneously for a same SKS phase. A measurement is considered valid if it is consistently rendered by different methods. Large measurement errors due to different methods can thus be ruled out. We used the SplitLab software package developed by Wüstefeld et al. (2008) to measure the shear wave splitting. The rotation correlation method (RC method, Bowman and Ando, 1987), minimum energy method (SC method, Silver and Chan, 1991), and eigenvalue method (EV method, Silver and Chan, 1991) were used to determine the fast polarization direction and the delay time, simultaneously.

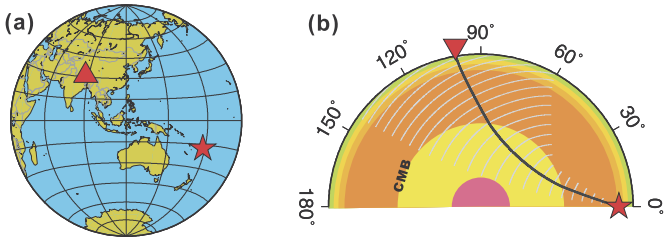

Fig. 2. Example for SKS-wave splitting analysis that makes reference to the event 2009313 recorded at the station C28 (see Tables 1 and 2 for locations of the station and the event). The Mw 7.3 earthquake was located at a depth of 585 km in the Tonga subduction zone. (a) Locations of station C28 (red triangle) and event 2009313 (red star). (b) Cross-section view of the SKS propagation path for the earthquake-station pair shown in (a). White arcs mark the positions of successive wavefronts at 60-s intervals along the SKS path.

3. Splitting results

An example of the outputs provided by the analysis for station C28 is shown in Fig. 3. The solution for the splitting parameters is given in the plot (b) and the intersection of the horizontal and vertical straight lines drawn in the plots (g) and (k), which provide the fast wave direction and the delay time, respectively. This procedure is systematically used in any other case.

3.1. Splitting parameters and travel times for a single event

Here we show variations of splitting parameters along the profile obtained from a single event 2009313. The event occurred on 9th November 2009 (Julian day 313) at UTC time 10h:44m:54s with a large magnitude of Mw 7.3. It is located in the Tonga subduction zone with a large focal depth of 585 km (Table 1 and Fig. 2). Clear SKS phases, well-separated from other phases, were recorded at almost all the stations with a high signal-to-noise ratio on both radial and transverse seismograms. The band-pass filtered radial- and transverse-component SKS waveforms are shown in Figs. 4a, 4b. The SKS waves have steep incidence angles ranging between 8.2° and 8.9° such as are calculated from the IASP91 model (Kennett and Engdahl, 1991), which leads to a high lateral resolution. The earthquake has similar backazimuths (103.3°–106.2°) and epicentral distances (96.394°–101.378°) along the profile (Fig. 4c).

The arrival times of SKS phases exhibit variations at stations close to the major rifts in the study area. We subtracted the theoretical travel times predicted by the IASP91 model from the SKS arrivals and picked the maximum-phase amplitudes on the radial-component (Fig. 4a). In the enlarged window (Fig. 4d), the SKS travel-time residuals are clearly related to locations of the rifts. The SKS arrivals between YGR and XDR is up to 2.5 s later than

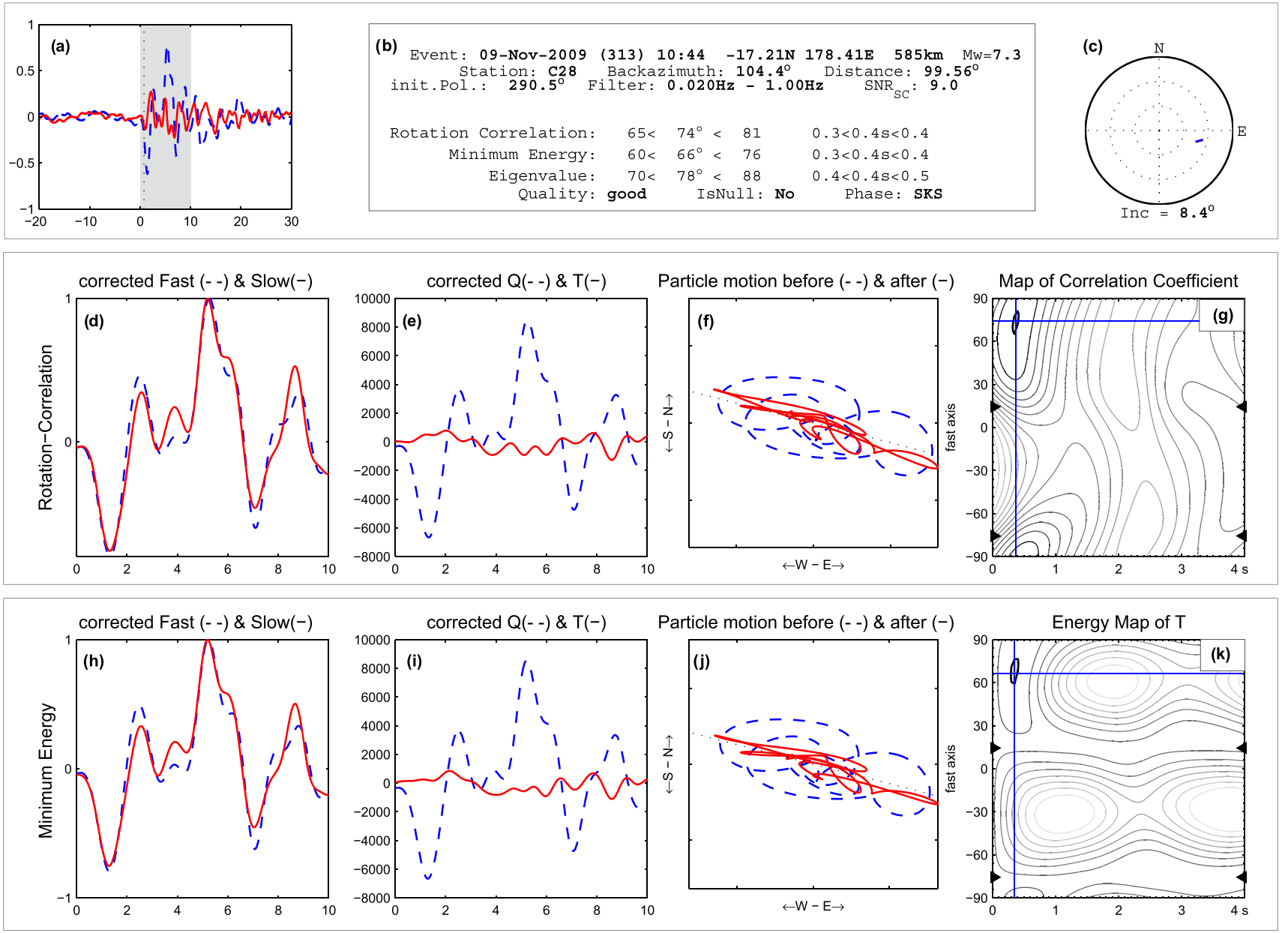

Fig. 3. Example of SKS-wave splitting measurement using the SplitLab software package (Wüstefeld et al., 2008) for event 2009313 recorded at station C28. Upper panels display the initial seismograms (a), information of the event-station pair and the measurement result (b), and the stereoplot (c) centered at station C28. Middle panels display result of the rotation-correlation (RC) technique: (d) seismogram components in fast (blue dashed) and slow (red solid) directions for RC-anisotropy system after RC-delay correction (normalized); (e) radial (Q, blue dashed) and transverse (T, red solid) components after RC-correction (not normalized); (f) particle motion before (blue dashed) and after (red solid) RC-correction; and (g) map of correlation coefficients. Lower panels display result of the minimum energy (SC) technique. Sub-plots (h)–(k) are similar with (d)–(g) in the middle panels.

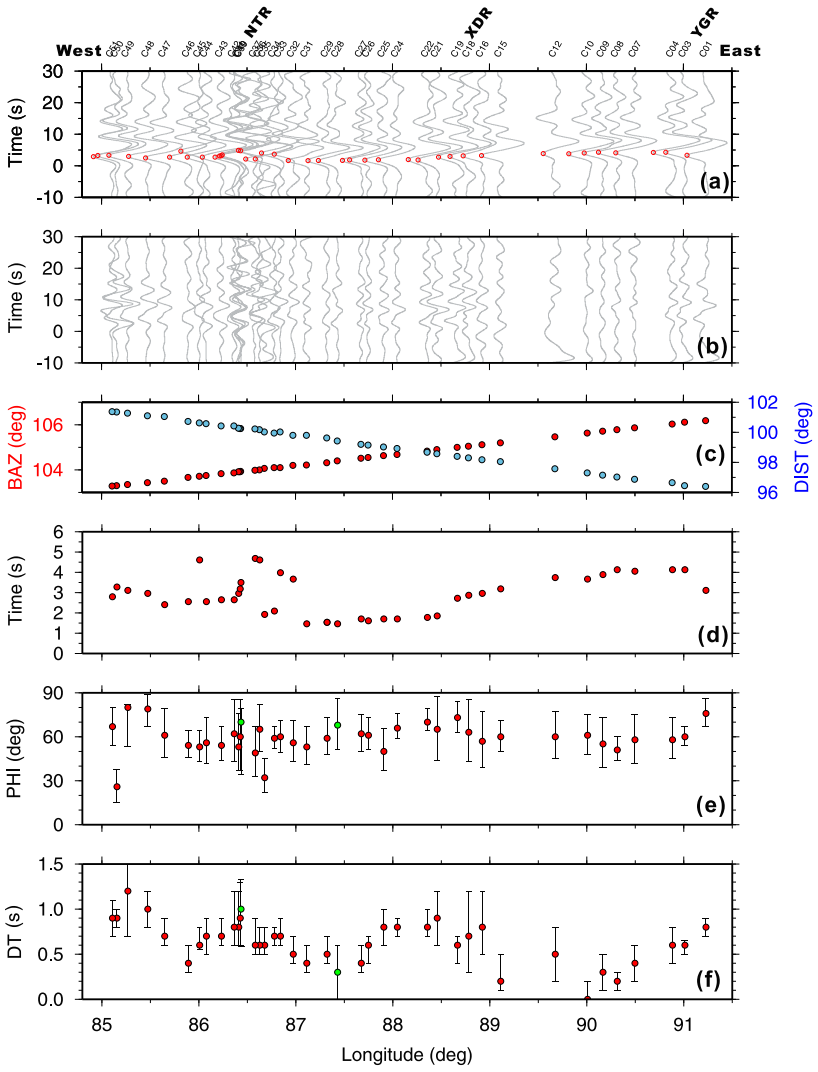

Fig. 4. SKS arrival times and splitting parameters for a single event. (a) Radial-component SKS waveforms generated by the event 2009313 recorded by all stations. Locations of stations and rifts are indicated on top. Red circles mark the maximum-amplitude picks of the SKS arrivals. Theoretical arrival times predicted by the IASP91 model (Kennett and Engdahl, 1991) are substracted. (b) The corresponding transverse-component records. (c) Backazimuths (red dots) and epicentral distances (blue dots). (d) Zoomed-in window of the relative SKS arrival times. (e) Fast polarization direction (PHI) of the SKS splitting measured by RC method at each station. (f) Delay time (DT) of the SKS splitting at each station. Vertical bars in (e) and (f) denote the error bounds marking the minimum and maximum range of the confidence region (Wüstefeld et al., 2008). Green dots mark the splitting parameters at stations C28 and C39, respectively. SKS-wave Fresnel zones of SKS waves for these two stations are illustrated in Fig. 6

the arrivals between XDR and NTR, and up to 1.5 s later than the arrivals west of NTR. Late SKS arrival indicates low shear wave velocities in the upper mantle.

As introduced in the last section, we use three different methods (RC, SC, and EV) to measure the SKS-wave splitting (Wüstefeld et al., 2008; Chen et al., 2013). We accept the results if similar splitting parameters are derived by different methods. The splitting parameters measured by RC method are shown in Fig. 4e, f. The fast wave polarization direction (PHI) is about 60° in average with a small fluctuation. The delay time (DT) shows long-wavelength variations (>150 km) related to the Yadong–Gulu Rift (YGR), Xainza–Dingjye Rift (XDR) and Nyima–Tingri Rift (NTR).

3.2. Splitting parameters and travel-time residuals for all events

We used the SplitLab software package (Wüstefeld et al., 2008) to measure the splitting of SKS phases for all the selected events and stations following the same procedure described above. There are more useful events for stations located in the west than those in the east (Fig. 5b) because of different data quality. The western stations are equipped with Reftek-130 logger, which is more reliable than its predecessor Reftek-72A used in the east. The average number of events used at each station is about 10.

We picked the SKS travel-time residuals on the radial-component at each station relative to station C18 for all the selected events used for splitting analysis (Fig. 5c) using AIMBAT software package (Lou et al., 2013), which is based on the multi-channel cross-correlation method (MCCC, VanDecar and Crosson, 1990). Compared to the SKS travel-time residuals for a single event (Fig. 4d), the station-averaged residuals for all selected events exhibit a similar tendency (Fig. 5c). Variations of the SKS travel-time residuals are clearly related to locations of the rifts. The SKS arrivals between YGR and XDR are up to 2.0 s later than the arrivals between XDR and NTR, and up to 1.0 s later than the arrivals west of NTR. This indicates that the upper mantle beneath the profile is divided by the rifts into different regions with different seismic velocity. The eastern part of the profile (between YGR and XDR) has the lowest velocity.

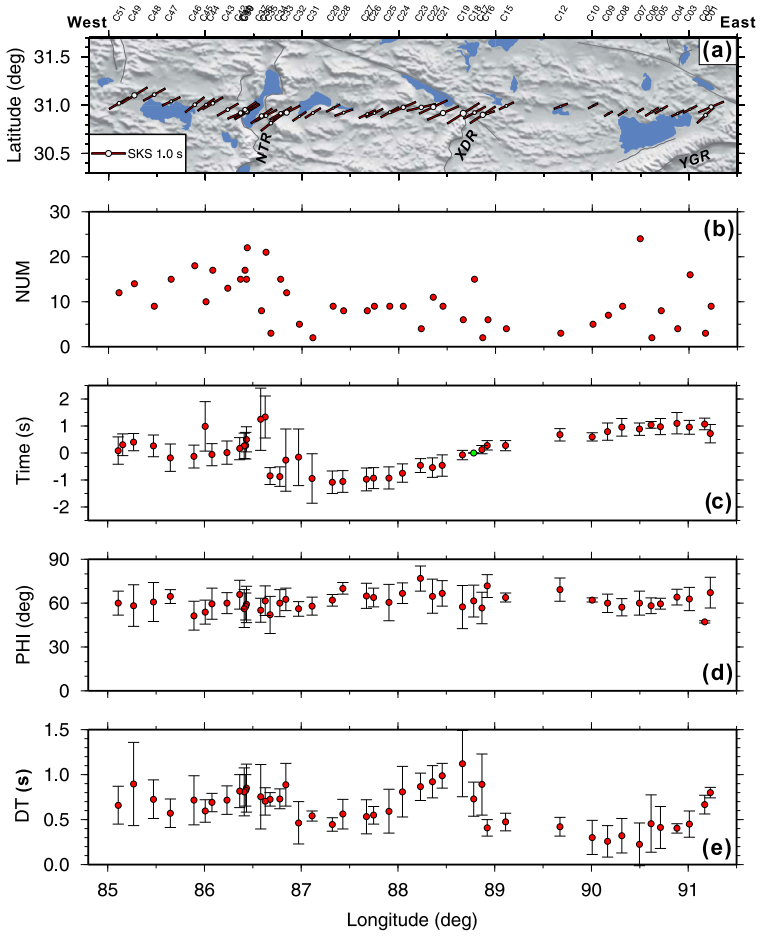

Fig. 5. Station-averaged travel-time residuals and splitting parameters of SKS waves for all events. (a) Topographic map of the surface with the splitting vectors associated to each station. The scale for the delay time of the SKS splitting is shown in the lower-left corner. (b) Number of useful events for travel-time residuals and SKS splitting measurements at each station. (c) Station-averaged travel-time residuals relative to station C18. (d) Station-averaged fast wave polarization directions. (e) Station-averaged splitting times. Vertical bars in (c), (d) and (e) denote the standard deviations of the arithmetic averages.

We then calculated the arithmetic average and standard deviations of the splitting parameters for each station (Table 2, Figs. 5d, 5e). Clear variations in shear wave splitting appear along the profile, which are closely related to locations of the north–south rifts. The averaged fast wave polarization direction at each station (PHI) shows an average of about 60° with a small fluctuation at the central part of the profile (close to ca. 70° between XDR and NTR). The delay times (DT) increase from 0.2 s in the east to 1.0 s in the west. The average delay time is small (about 0.3 s) between YGR and XDR, intermediate (about 0.5 s) between XDR and NTR, and increases to 0.7 s west of NTR.

The delay times (DT) show a rapid increase in the vicinity of the rifts (Fig. 5e), suggesting a significant contribution of the rifts to the shear-wave splitting. On one hand, the splitting delay time depends both on the degree of anisotropy and on the thickness of the anisotropic layer in which the shear wave propagates. On the other hand, for the same degree of anisotropy a lower isotropic velocity can result in a larger delay time between the fast and slow waves. However, the SKS arrival time residuals do not show clearly rift-related variations (Fig. 5c). In the vicinity of the rifts, only NTR exhibits larger travel time residuals of SKS waves. No rapid change in the travel-time residuals is discernible at the other rifts further east (XDR and YGR). We therefore tend to believe that the larger splitting delay times in the vicinity of rifts are mainly induced by the anisotropy in the rifts.

3.3. Fresnel zone calculation

Alsina and Snieder (1995) proposed a method to constrain the depth of the anisotropy by using Fresnel zones of SKS phases. The basic idea is that the different splitting observations at two closely located stations are mainly contributed by the non-overlapped part of the Fresnel zones. Following this idea, we calculated the Fresnel zones at stations C28 and C39 (green dots in Fig. 4e, f) for the same event 2009313 (Fig. 2). These two stations were selected not only because both of them have continuous and reliable observations, but also because they have different splitting parameters. They thus represent an example of a large lateral variation of anisotropy. As a first-order approximation in our calculations, we used the IASP91 model (Kennett and Engdahl, 1991) and the TauP Toolkit (Crotwell et al., 1998) to trace the ray path and to calculate the first Fresnel zone by emitting a narrow ray-beam from the wavefront of the SKS phase to the stations (Fig. 6a). The Fresnel zone width at different depth is bounded by rays, whose arrival times fall within $\pm T/6$ of the arrival time of the SKS phase, T being the dominant period that usually is assumed to be 8 s for SKS phase (Alsina and Snieder, 1995; Özazlaybey and Chen, 1999; Favier and Chevrot, 2003; Liu and Gao, 2011). Fig. 6 shows the first Fresnel zones in a cross-section view. In this case both zones for the two stations overlap at a depth greater than about 195 km (Fig. 6b). Therefore, we argue that the main source of anisotropy should be located above this depth.

Table 2
Results from the SKS splitting analysis and travel-time measurements at stations of the TIBET-31 N seismic array[a]

Station	Latitude (°N)	Longitude (°E)	FPD (deg.)	Delay time (s)	Travel-time residual (s)	No. of events
C01	30.9834	91.2300	67.15 ± 10.45	0.80 ± 0.06	0.72 ± 0.34	9
C02	30.8967	91.1718	47.20 ± 0.82	0.67 ± 0.10	1.07 ± 0.22	3
C03	30.9601	91.0133	62.86 ± 7.88	0.45 ± 0.14	0.95 ± 0.26	16
C04	30.9155	90.8839	64.11 ± 5.39	0.40 ± 0.05	1.10 ± 0.40	4
C05	30.9553	90.7156	59.61 ± 3.66	0.41 ± 0.23	0.97 ± 0.30	8
C06	30.9323	90.6170	58.22 ± 5.30	0.46 ± 0.32	1.04 ± 0.12	2
C07	30.9476	90.4958	60.03 ± 8.27	0.23 ± 0.24	0.88 ± 0.23	24
C08	30.9256	90.3172	57.26 ± 5.89	0.32 ± 0.19	0.95 ± 0.32	9
C09	30.9117	90.1674	59.90 ± 6.36	0.26 ± 0.18	0.79 ± 0.32	7
C10	30.9925	90.0098	62.15 ± 1.45	0.30 ± 0.19	0.60 ± 0.16	5
C12	30.9915	89.6766	69.26 ± 7.90	0.42 ± 0.10	0.67 ± 0.23	3
C13	30.9161	89.5590	–	–	–	
C14	30.9119	89.4003	–	–	–	
C15	30.9947	89.1130	63.91 ± 3.01	0.47 ± 0.10	0.27 ± 0.19	4
C16	30.9172	88.9223	71.67 ± 7.71	0.41 ± 0.09	0.28 ± 0.18	6
C17	30.8995	88.8685	56.75 ± 10.79	0.89 ± 0.34	0.12 ± 0.15	2
C18	30.9252	88.7859	$61, 42 \pm 10.99$	0.73 ± 0.19	0	15
C19	30.9153	88.6680	57.35 ± 14.73	1.12 ± 0.37	-0.07 ± 0.17	6
C20	30.9154	88.5686	–	–	–	
C21	30.9200	88.4589	66.66 ± 8.75	0.99 ± 0.14	-0.46 ± 0.39	9
C22	30.9835	88.3575	64.74 ± 11.77	0.92 ± 0.18	-0.55 ± 0.36	11
C23	30.9773	88.2333	76.84 ± 8.57	0.87 ± 0.15	-0.46 ± 0.26	4
C24	30.9801	88.0491	66.77 ± 6.95	0.81 ± 0.28	-0.75 ± 0.34	9
C25	30.9262	87.9098	60.39 ± 12.51	0.59 ± 0.24	-0.93 ± 0.41	9
C26	30.9202	87.7489	63.87 ± 6.45	0.55 ± 0.10	-0.93 ± 0.39	9
C27	30.9092	87.6757	64.96 ± 8.55	0.53 ± 0.19	-0.98 ± 0.42	8
C28	30.9245	87.4334	70.13 ± 4.06	0.56 ± 0.17	-1.06 ± 0.40	8
C29	30.9715	87.3226	61.99 ± 3.97	0.45 ± 0.08	-1.08 ± 0.42	9
C31	30.9192	87.1139	57.98 ± 6.13	0.54 ± 0.06	-0.95 ± 0.92	2
C32	30.8851	86.9752	56.04 ± 5.10	0.46 ± 0.24	-0.16 ± 1.04	5
C33	30.9232	86.8436	62.59 ± 7.60	0.89 ± 0.24	-0.26 ± 1.15	12
C34	30.9156	86.7799	60.00 ± 9.31	0.73 ± 0.11	-0.88 ± 0.37	15
C35	30.8140	86.6802	$51, 94 \pm 12.71$	0.73 ± 0.08	-0.85 ± 0.31	3
C36	30.8938	86.6293	61.65 ± 10.19	0.70 ± 0.15	1.33 ± 0.78	21
C37	30.8907	86.5823	55.05 ± 8.23	0.76 ± 0.36	$1, 25 \pm 1.15$	8
C39	30.9320	86.4375	59.20 ± 12.45	0.85 ± 0.27	0.50 ± 0.47	22
C40	30.9398	86.4262	57.64 ± 9.24	0.83 ± 0.18	0.27 ± 0.50	15
C41	30.9537	86.4114	56.23 ± 12.96	0.81 ± 0.27	0.26 ± 0.47	17
C42	30.9198	86.3658	65.87 ± 9.90	0.82 ± 0.18	0.16 ± 0.41	15
C43	30.9538	86.2346	60.01 ± 7.25	0.72 ± 0.16	0.01 ± 0.43	13
C44	31.0219	86.0792	59.53 ± 10.60	0.69 ± 0.10	-0.06 ± 0.41	17
C45	31.0071	86.0104	53.84 ± 8.15	0.60 ± 0.12	0.99 ± 0.92	10
C46	31.0041	85.8941	51.37 ± 9.96	0.72 ± 0.27	-0.13 ± 0.42	18
C47	31.0407	85.6490	64.54 ± 4.82	0.57 ± 0.16	-0.18 ± 0.51	15
C48	31.1109	85.4732	60.75 ± 13.23	0.73 ± 0.22	0.26 ± 0.40	9
C49	31.1043	85.2698	58.30 ± 14.22	0.89 ± 0.46	0.40 ± 0.32	14
C50	31.0219	85.1580	30.98 ± 8.29	1.09 ± 0.51	0.31 ± 0.40	3
C51	31.0223	85.1102	60.00 ± 8.25	0.66 ± 0.21	0.09 ± 0.50	12

[a] Results are not given for stations with no available data. Station-averaged travel-time residuals are relative to station C18.

4. Discussion

4.1. Origin of the seismic anisotropy in Tibet

In Fig. 7 we compare our shear wave splitting results with a collection of previous data (McNamara and Owens, 1994; Hirn et al., 1995, 1998; Lave et al., 1996; Sandvol and Ni, 1997; Herquel and Tapponnier, 2005; Flesch et al., 2005; Sol et al., 2007; Huang et al., 2000; Fu et al., 2008; Wang et al., 2008; Kumar and Singh, 2008; Gao and Liu, 2009; Chen et al., 2010a; Zhao et al., 2010, 2014). Most of the splitting data are downloaded from the online database (http://splitting.gm.univ-montp2.fr/DB; Wüstefeld et al., 2009). A few more are extracted from published papers. Some (but not all) very small splittings (<0.2 s), considered as null cases by the original authors, are plotted as null birefringence here, too. The shear wave splitting results are combined with main tectonic features, GPS velocities with respect to stable Eurasia (Zhang et al., 2004) and the Absolute Plate Movement (APM) calculated from http://www.sps.unavco.org using the GSRM V1.2 model (Kreemer et al., 2003). In general, our splitting features are well consistent with and complementary to the results from previous studies performed in southern Tibet.

Previous studies found that there is null or very weak splitting (Fig. 7) beneath the Himalayas and southernmost Lhasa block and interpreted the onset of splitting as an indicator for the frontier of the northwards advancing Indian lithosphere beneath Tibet (e.g., Sandvol and Ni, 1997; Fu et al., 2008; Huang et al., 2000). However, the mechanism is still unclear. There are three possibilities to explain the lack of resolvable seismic anisotropy beneath southernmost Tibet (Huang et al., 2000). The first one is a Lattice Preferred Orientation (LPO) fabric with a subvertical symmetry axis in the underlying Indian lithosphere, which could be produced by the present-day thickened and downwelling (vertical elongation) of the Indian lower lithosphere (Sandvol and Ni, 1997) or by the corner flow and shear at the base of the Indian lower lithosphere (Fu et al., 2008) beneath southern Tibet. Another possibility is that the underthrusting Indian lithosphere beneath southern Tibet simply lacks a coherent LPO fabric (Chen and Özalaybey, 1998; Özalaybey and Chen, 1999; Huang et al., 2000; Chen et al., 2010a), as is the case in the Indian shield. The third

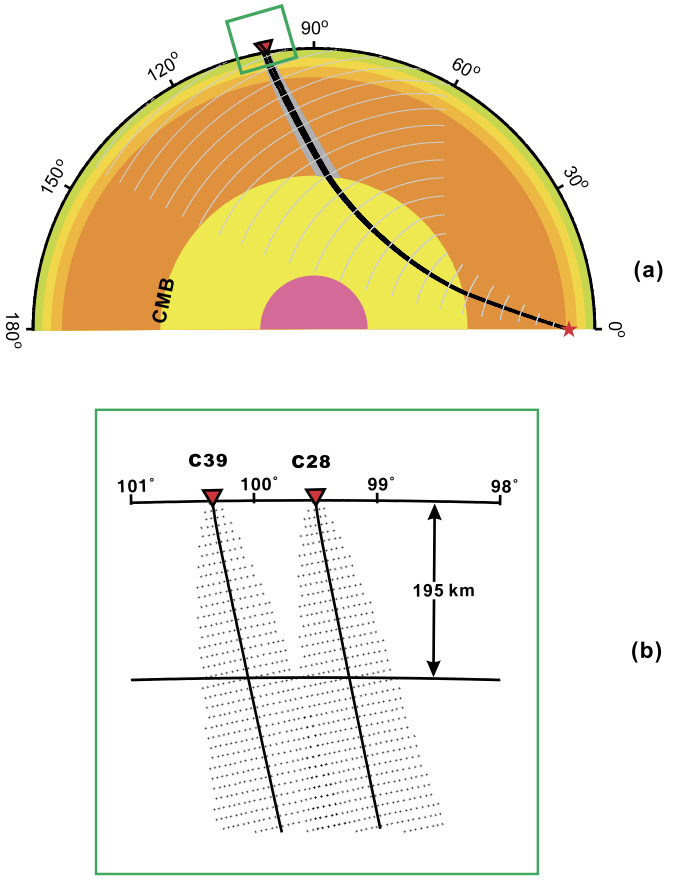

Fig. 6. Cross-section view of SKS-wave Fresnel zones calculated for event 2009313 recorded at stations C28 and C39, indicated in Fig. 4e, f. (a) SKS paths for the two earthquake-station pairs in the Earth. Gray arcs mark the positions of successive wavefronts at 60-s intervals. (b) The enlarged zone outlined by the green square box in (a). Dotted lines mark the positions of successive wavefronts at 2-s intervals. Notice that the SKS-wave Fresnel zones for both branches are overlapped at depths deeper than about 195 km. As a first-order approximation the global Earth model IASP91 (Kennett and Engdahl, 1991) was used in the calculations.

model is that anisotropy in the Indian lithosphere and in the underlying asthenosphere are oriented in different directions with a big angle, thus effectively resulting in a null birefringence. The latter two models are based on the observations of null splitting at stations in the Indian plate (e.g., Chen and Özalaybey, 1998). However, many other measures of splitting made more recently at stations in India show large splitting (close to 1 s) and most of the azimuths corresponding to fast polarization direction can be explained by the APM-related strain (Kumar and Singh, 2008; Kumar et al., 2010; Saikia et al., 2010). So the latter two explanations employing a weak anisotropic Indian plate are unlikely to be true. In fact, most of the previous studies suggested that the splitting in Tibet is mainly originated from the mantle convection flow in the asthenosphere, which is related to the APM of Eurasia (McNamara and Owens, 1994; Hirn et al., 1995, 1998; Lave et al., 1996; Gao and Liu, 2009; Huang et al., 2000).

In the Indian shield, the fast polarization direction is aligned in the NNE direction, consisting with the Indian Plate motion approximately (Kumar and Singh, 2008; Kumar et al., 2010; Saikia et al., 2010). The dominant fast speed direction of 60° along our profile is similar to that observed in the Indian shield, implying a same source of anisotropy induced by the asthenospheric flow beneath the downgoing Indian plate. Alternatively the corner flow in the overlying mantle wedge induced by downdip motion of the Indian slab may contribute to the observed anisotropy in the same direction.

With the caution that the splittings represent vertically integrated point measurements, whereas surface waves average horizontally over large distances, the comparison of both types of anisotropy based on the L–R discrepancy or else on shear wave splitting can be done with care (Wüstefeld et al., 2009). Under the simplest assumption of a vertical symmetry axis, the area with relatively strong radial anisotropy should have weak or no azimuthal anisotropy. The central Lhasa block has strong radial anisotropy (Chen et al., 2009) but weak azimuthal anisotropy within the upper mantle, which implies a subvertical orientation of α axis caused by the subduction of the Indian Plate (Savage, 1999).

4.2. Lateral variations of the subduction-related mantle structure

The 2000 km-long east–west Himalayan–Tibetan collision zone is in a complex tectonic setting consisting of six major tectonic domains (Yin, 2010). The shortening in the Cenozoic deformation estimated from geological observations in the Himalayan orogen shows several hundred kilometers with distinct lateral variations (Yin, 2010), which is also confirmed by the differential movement constrained by the present-day GPS data (Fig. 7). It would be very hard to keep a uniform geometry during such a large-scale collision accompanied by subduction in a so complex tectonic setting. Many geophysical observations have already provided insights into the significant lateral variations in the subduction-related mantle structure beneath this collision zone. The geometry and the nature of the subduction of the Indian plate may change distinctly in certain places. For example, the Indian plate is subducting eastward and sinks into the mantle transition zone along the Burma arc (Li et al., 2008; Lei et al., 2009), which is very different from the main Himalayan–Tibetan collision zone. Combining seismic images derived by different techniques, such as body wave tomography (Tilmann et al., 2003; Zhou and Murphy, 2005; Li et al., 2008; He et al., 2010; Liang et al., 2012; Zhao et al., 2013), surface wave tomography (Brandon and Romanowicz, 1986; Priestley et al., 2006; Chen et al., 2010b; Li et al., 2013), receiver functions (Yuan et al., 1997; Kosarev et al., 1999; Kind et al., 2002; Kumar et al., 2006; Nabelek et al., 2009; Zhao et al., 2010; Zhao et al., 2011) and controlled-source seismic investigations (Zhao et., 1993), it has been suggested that the horizontal sliding distance of the Indian lithosphere under the Tibetan Plateau from west to east (Kind and Yuan, 2010) and that the dip angle of the subducting Indian lithosphere varies laterally (Zhou and Murphy, 2005; Li et al., 2008).

4.3. Mechanism for lateral variations of the subduction

A mechanism is needed to accommodate the significant lateral variations of the geometry and the nature of the subducting India lithospheric slab. Based on the data of the rift spaces, the age of rift initiation, and the instability analysis, Yin (2000) proposed a model, in which the Indian mantle lithosphere directly beneath the Himalaya is involved in east–west extension in Tibet and the rifts occur in the subducting Indian lithosphere. By comparing the differences in lithospheric structure, magmatism and deformation styles between western and eastern Tibet, Xiao et al. (2007) proposed a slab-tearing model in which the Indian lithosphere has been split into two parts separated by YGR: a part subducting northward steeply beneath the western plateau, and a northeastward subducting one with shallow angle beneath the eastern plateau. According to the features of the Gandese tectonomagmatic belt and the aeromagnetic anomalies in Tibet, Hou et al. (2006) suggested that the tearing of the Indian lithosphere probably resulted in dischronal subduction along the Indo-Asian collision zone. Mahéo et al. (2002) argued that the Neogene magmatic and metamorphic evolution of the South Asian margin was controlled

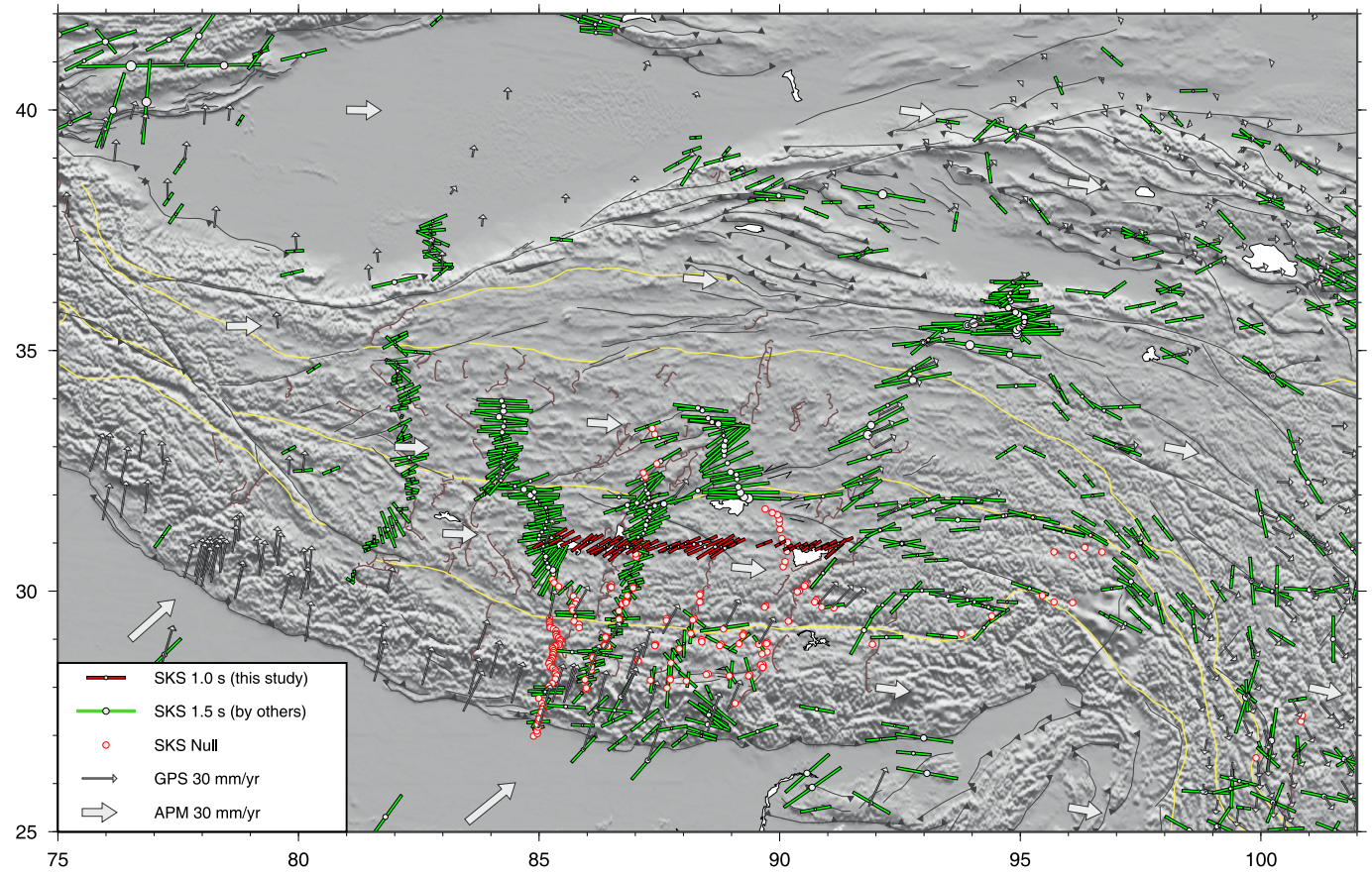

Fig. 7. Shear-wave splitting vectors extracted from previous research works (green bars) together with those obtained in this study (red bars), they all drawn on a topographic map with geological features of the explored region. Thin arrows denote GPS velocities with respect to stable Eurasia (Zhang et al., 2004). Thick arrows indicate the Absolute Plate Motions (APM), calculated by the Plate Motion Calculator from http://www.sps.unavco.org using the GSRM V1.2 model (Kreemer et al., 2003). SKS/SKKS splitting measurements are collected from McNamara and Owens (1994), Hirn et al. (1995), Lave et al. (1996), Sandvol and Ni (1997), Hirn et al. (1998), Herquel and Tapponnier (2005), Flesch et al. (2005), Sol et al. (2007), Huang et al. (2000), Fu, et al., 2008, Wang et al. (2008), Kumar and Singh (2008), Gao and Liu (2009); Chen et al. (2010a), Zhao et al. (2010, 2014). Most of them were downloaded from the online database at http://splitting.gm.univ-montp2.fr/DB (Wüstefeld et al., 2009). Note that some (but not all) very weak splittings (<0.2 s) were simply looked as the null cases by the original authors, and here they are plotted as null birefringence, too.

by slab breakoff of the subducting Indian continental margin starting at about 25 Ma. This model is supported by the adakitic intrusive generated during the mid-Miocene extension in southern Tibet (Hou et al., 2004). Besides these geological and geochemical observations, the tearing of the Indian mantle lithosphere underneath southern Tibet is also supported by seismological evidences. Liang et al. (2011) carried out a finite-frequency body wave tomography to image the 3-D upper mantle velocity structure beneath southern Tibet. They suggested that the Indian mantle lithosphere has been broken laterally in the direction perpendicular to the convergence beneath the north–south oriented rifts, and subducted progressively in a piecewise way and subparallel to the current one beneath the High Himalaya. The fragmented Indian slab is also supported by a later study of Rayleigh-wave tomography with a 2-D seismic array in southern Tibet (Jiang et al., 2011), and by another study using finite-frequency tomography with more combined data in eastern Tibet (Liang et al., 2012). Therefore, the slab tearing and/or the slab breakoff of the subducted Indian lithosphere likely are probably the most plausible mechanism to accommodate the significant lateral variations of the northward subduction.

We observe several first-order features from our shear-wave splitting study along profile TIBET-31N. 1) The delay times of SKS splitting vary between 0.2 s and 1.0 s and increase from east to west. The profile can be divided into different segmentations by the north–south trending rifts (Figs. 4, 5, and 7). 2) The SKS travel-time residuals from a single event (Fig. 4a, d) and all selected events (Fig. 5c) show later arrivals in the east than in the west. 3) The depth of the anisotropy is estimated to be above 195 km (Fig. 6). All these features suggest that the geometry of the northward subducting Indian lithosphere in the Himalayan–Tibetan collision zone beneath southern Tibet may have systematic lateral variations from east to west. We propose a slab-tear and/or breakoff model with different subduction angles to explain these east–west variations (Fig. 8). Under the assumption that the shear wave splitting in Tibet is mainly originated from the mantle convection flow in the asthenosphere, the strength of seismic anisotropy would depend on the subvertical mantle shear strain field caused by the downwelling of the asthenospheric flow in his turn controlled by the variable dip angle of the Indian lithosphere. Underneath the eastern part of the profile (between YGR and XDR, Fig. 5a), the Indian lithospheric slab is subducted at a steep angle and does not extend further north. The steep subduction is associated with a subvertical downwelling asthenospheric flow that results in null or very weak splitting (ca. 0.3 s) (Fig. 4f and Fig. 5e). Meanwhile, the thickened asthenospheric mantle wedge above the steep subducting Indian lithosphere, and/or the upwelling asthenospheric flow induced by the slab breakoff (Davies and von Blanckenburg, 1995; Maheo et al., 2002; Hou et al., 2004; van Hunen and Allen, 2011) would result in slow seismic velocity, which would be consistent with later SKS arrival times in this region (Fig. 4d; Fig. 5c). Underneath the central part of the profile (between XDR and NTR, Fig. 5a), the Indian lithospheric slab is

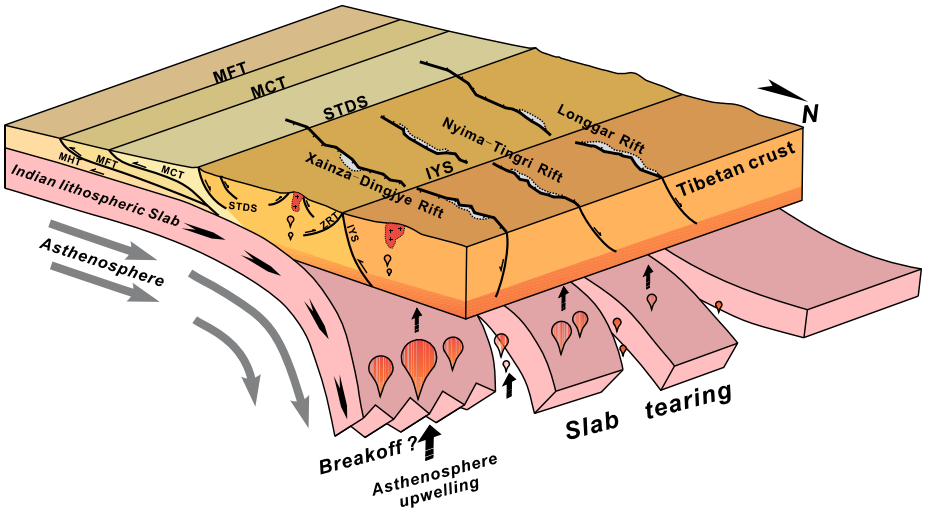

Fig. 8. Interpretation cartoon showing the slab tearing and/or breakoff model of the Indian lithosphere with differential subduction angles in the Himalayan–Tibetan collision zone. Acronyms: MFT, Main Frontal Thrust; MCT, Main Central Thrust; STDS, Southern Tibetan detachment systems; ZRT, Zedong–Renbu Thrust; IYS, Indus–Yarlung suture. The dip angle of the northward advancing Indian lithospheric slab is decreasing from east to west with tears at the north–south rift strikes. Hence, the Indian plate has reached farther north in the west.

subducted with a shallower angle than the east part, and thus extends further north than the east part. The low-angle subduction introduced an asthenospheric flow with an apparent horizontal flow component thus inducing larger splittings (ca. 0.5 s) than the east portion of the profile. West of NTR (Fig. 5a), the subducting angle of the Indian lithosphere is even flatter resulting in strong SKS splittings (ca. 0.7 s). Here the underthrusting Indian plate has reached the farther north of Tibet. The changing geometry of the subducted Indian lithosphere is accommodated by the slab tearing in the direction perpendicular to the convergence, which is correlated with the north–south oriented rifts (Fig. 8). The front of the Indian plate reaches farther north in the west than in the east. This scenario is supported not only by the features of our splitting measurements and arrival times of SKS waves, but also by the evidence from many previous geological and geochemical observations discussed above.

It must be assumed that complex slab morphology as we propose here would affect the mantle flow and likely also would complicate the resulting anisotropy (Kneller and van Keken, 2007; Hanna and Long, 2012). To identify the most reliable first-order features of our data set, we measured SKS splitting parameters and travel-time residuals using events only within a narrow back-azimuth and epicentral distance band. We then computed the station-averaged splitting parameters and travel-time residuals to achieve enough clear observations influenced as little as possible by random errors, and eventually it is physically meaningful to constrain the studied deep process. Despite the notable simplification of the data processing, the splitting parameters and travel-time residuals show rapid changes with larger deviations close to the rifts (Fig. 5). These features associated to the rifts suggest a complicated anisotropy pattern and a complicated deep process within the tearing window on a narrow lateral scale. The simplification and the measurement errors within a small lateral space restrain the discussion of splitting tearing-related in more detail.

4.4. The cause of slab tearing

The northward moving Indian lithospheric slab ploughs the upper mantle beneath southern Tibet (Cox and Hart, 1986; Kearey and Vine, 1996; Müller, 2007). As discussed in Section 4.2, either the physical property or the dynamic setting of the subducting Indian lithosphere should be far from homogeneous, resulting in kinematic differences within a plate. Modifications of the physical property in the subducting slab and/or severely accumulated strain within the slab can provide a locus for incipient tears (Kennett and Furumura, 2010). If the accumulated strain is beyond the strength of the plate, the slab will break into segmentations along internal weaknesses (Rosenbaum et al., 2008). Slab tearing plays a key role in the development of segmented subduction. There are two types of tears according to their propagating directions (Rosenbaum et al., 2008). A horizontal tear propagates in the direction perpendicular to the convergence, usually leading to *slab delamination* (slab breakoff) due to gravity instability as the scenario we propose beneath the east part of the profile (Fig. 8). A vertical tear propagates subparallel to the convergence direction, usually leading to *slab detachment* (slab splitting) due to the shear tear from differential rollback velocities as the scenario we propose beneath the central and west parts of the profile (Rosenbaum et al., 2008; Huang et al., 2010). In the literature *slab breakoff* is commonly referred to the former case, while *slab tearing* is the latter one. The dip angle of the segmented slab plays a virtual role to control the kinematic characteristics of the subducting slab. It is easy to understand that a slab with a shallow angle has major movements on the horizontal component and can extend to a farther distance, while a slab with a steep angle has major movement on the vertical component and can descend to a deeper depth. The positive-feedback between the dip angle and differential slab movement enhances the differentiation between the moving slabs, so that the dip angle of a subducting slab may ultimately decide its fate in kinematics. Within a huge subducting plate, the slab tearing often occurs among differential movements of segmentations, which leads to a scenario of divergent fingers with differential geometry (Fig. 8).

5. Conclusions

SKS splitting along an east–west trending seismic array in Lhasa block revealed significant lateral variations. The fast polarization directions are close to 60° along the profile with small fluctuations. The delay times increase from east to west between 0.2 s and 1.0 s with strong changes corresponding to the north–south oriented rifts in southern Tibet. The depth of anisotropy is estimated to be above about 195 km according to the Fresnel zones calculation. The SKS travel-time residuals show larger time lags (1.0–2.0 s) in the eastern transect of the profile, indicating low velocities in the underlying upper mantle. All these observations, analyzed as a

whole, suggest systematic lateral variations in the geometry of the underthrusting Indian lithosphere in the Himalayan–Tibetan collision zone beneath southern Tibet. A slab tearing and/or breakoff model with different subduction angles is a good candidate to explain our observations.

Acknowledgements

We would like to express the most sincere respect and the most deep memory to the former group leader and good friend, Prof. Zhongjie Zhang, who suddenly passed away in September 6th, 2013. It was Zhongjie who led, together with other colleagues, most of the fieldworks and research projects in Tibet undertaking by the group, including the deployment of the TIBET-31N seismic array. We would like to thank Drs. Tao Xu, Changqing Sun, Shaokun Si, Haiqiang Lan, and the vehicle drivers, Bianba and Duoji, and other field personnel for collecting the high quality data in the hard conditions of central Tibet. We also wish to thank Profs. Yanghua Wang, Bihong Fu, Rui Gao, Fuqin Zhang, Carlos López Casado for their helpful discussions, and Profs. Xiaofeng Liang, Xiaobo Tian for significant improvement of the manuscript. Constructive comments and suggestions from anonymous reviewers significantly improved the quality of this paper. All figures were produced using the Generic Mapping Tools software package (Wessel and Smith, 1998). The Strategic Priority Research Program (B) of Chinese Academy of Sciences (grant XDB03010700) and Sinoprobe-02-03 funded the TIBET-31N project. This research is also supported by the National Natural Science Foundation of China (grants 41374063 and 40830315). The Seismic Array Laboratory, IGGCAS, provided the instrumental equipment.

References

Alsina, D., Snieder, R., 1995. Small-scale sublithospheric continental mantle deformation: constraints from SKS splitting observations. Geophys. J. Int. 123, 431–448.

Bowman, J.R., Ando, M., 1987. Shear-wave splitting in the upper-mantle wedge above the Tonga subduction zone. Geophys. J. R. Astron. Soc. 88, 25–41.

Brandon, C., Romanowicz, B., 1986. A no-lid zone in the central Chang–Tang platform of Tibet – evidence from pure path phase-velocity measurements of long period Rayleigh-waves. J. Geophys. Res. 91 (B6), 6547–6564.

Chen, W.P., Özalaybey, S., 1998. Correlation between seismic anisotropy and Bouguer gravity anomalies in Tibet and its implications for lithospheric structures. Geophys. J. Int. 135, 93–101.

Chen, Y., Badal, J., Zhang, Z., 2009. Radial anisotropy in the crust and upper mantle beneath the Qinghai–Tibet Plateau and surrounding regions. J. Asian Earth Sci. 36, 289–302.

Chen, W.P., Martin, M., Tseng, T.L., Nowack, R.L., Hung, S.H., Huang, B.S., 2010a. Shear-wave birefringence and current configuration of converging lithosphere under Tibet. Earth Planet. Sci. Lett. 295, 297–304.

Chen, Y., Badal, J., Hu, J.F., 2010b. Love and Rayleigh wave tomography of the Qinghai–Tibet Plateau and surrounding areas. Pure Appl. Geophys. 167, 1171–1203.

Chen, Y., Zhang, Z.J., Sun, C.Q., Badal, J., 2013. Crustal anisotropy from Moho converted Ps wave splitting analysis and geodynamic implications beneath the eastern margin of Tibet and surrounding regions. Gondwana Res. 24 (3–4), 946–957.

Cox, A., Hart, R.B., 1986. Plate Tectonics: How It Works. Blackwell Science, Oxford, UK, pp. 337–351.

Crotwell, H.P., Owens, T.J., Ritsema, J., 1998. The TauP ToolKit: flexible seismic traveltime and raypath utilities. Seismol. Res. Lett. 70, 154–160.

Davies, J.H., von Blanckenburg, F., 1995. Slab breakoff: a model of lithosphere detachment and its test in the magmatism and deformation of collisional orogens. Earth Planet. Sci. Lett. 129, 85–102.

Dewey, J.F., Burke, K., 1973. Tibetan, Variscan and Precambrian basement reactivation: products of continental collision. J. Geol. 81, 683–692.

Favier, N., Chevrot, S., 2003. Sensitivity kernels for shear wave splitting in transverse isotropic media. Geophys. J. Int. 153, 213–228.

Flesch, L.M., Holt, W.E., Silver, P.G., Stephenson, M., Wang, C.Y., Chan, W.W., 2005. Constraining the extent of crust-mantle coupling in central Asia using GPS, geologic, and shear wave splitting data. Earth Planet. Sci. Lett. 238, 248–268.

Fu, Y.V., Chen, Y.J., Li, A.B., Zhou, S.Y., Liang, X.F., Ye, G.Y., Jiang, M.M., Ning, J.Y., 2008. Indian mantle corner flow at southern Tibet revealed by shear wave splitting measurements. Geophys. Res. Lett. 35, L02308. http://dx.doi.org/10.1029/2007GL031753.

Gao, S.S., Liu, K.H., 2009. Significant seismic anisotropy beneath the southern Lhasa Terrane, Tibetan Plateau. Geochem. Geophys. Geosyst. 10 (2), Q02008. http://dx.doi.org/10.1029/2008GC002227.

Hanna, J., Long, M.D., 2012. SKS splitting beneath Alaska: regional variability and implications for subduction processes at a slab edge. Tectonophysics 530–531, 272–285.

He, R.Z., Zhao, D.P., Gao, R., Zheng, H.W., 2010. Tracing the Indian lithospheric mantle beneath central Tibetan Plateau using teleseismic tomography. Tectonophysics 491, 230–243.

Herquel, G., Tapponnier, P., 2005. Seismic anisotropy in western Tibet. Geophys. Res. Lett. 32, L17306. http://dx.doi.org/10.1029/2005GL023561.

Hirn, A., Jiang, M., Sapin, M., Diaz, J., Nercessian, A., Lu, Q.T., Lepine, J.C., Shi, D.N., Sachpazl, M., Pandey, M.R., Ma, K., Gallart, J., 1995. Seismic anisotropy as an indicator of mantle flow beneath the Himalayas and Tibet. Nature 375 (15), 571–574.

Hirn, A., Diaz, J., Sapin, M., Veinante, J.L., 1998. Variation of shear-wave residuals and spitting parameter from array observations in southern Tibet. Pure Appl. Geophys. 151, 407–431.

Hou, Z.Q., Gao, Y.F., Qu, X.M., Rui, Z.Y., Mo, X.X., 2004. Origin of adakitic intrusive generated during mid-Miocene east–west extension in southern Tibet. Earth Planet. Sci. Lett. 220, 139–155.

Hou, Z.Q., Zhao, Z.D., Gao, Y.F., Yang, Z.M., Jiang, W., 2006. Tearing and dischronal subduction of the Indian continental slab: evidence from Cenozoic Gangdese volcano-magmatic rocks in south Tibet. Acta Petrol. Sin. 22 (4), 761–774 (in Chinese with abstract in English).

Huang, W.C., Ni, J.F., Tilmann, F., Nelson, D., Guo, J.R., Zhao, W.J., Mechie, J., Kind, R., Saul, J., Rapine, R., Hearn, T.M., 2000. Seismic polarization anisotropy beneath the central Tibetan Plateau. J. Geophys. Res. 105 (B12), 27979–27989.

Huang, J.P., Vanacore, E., Niu, F.L., Levander, A., 2010. Mantle transition zone beneath the Caribbean–South American plate boundary and its tectonic implications. Earth Planet. Sci. Lett. 289, 105–111.

Jiang, M.M., Zhou, S.Y., Sandvol, E., Chen, X.F., Liang, X.F., Chen, Y.J., Fan, W.Y., 2011. 3-D lithospheric structure beneath southern Tibet from Rayleigh-wave tomography with a 2-D seismic array. Geophys. J. Int. 185, 593–608.

Kearey, P., Vine, F.J., 1996. Global Tectonics, 2nd edition. Blackwell Science, Oxford, UK, pp. 248–262.

Kennett, B.L.N., Engdahl, E.R., 1991. Traveltimes for global earthquake location and phase identification. Geophys. J. Int. 105, 429–465.

Kennett, B.L.N., Furumura, T., 2010. Tears or thinning? Subduction structures in the Pacific plate beneath the Japanese Islands. Phys. Earth Planet. Inter. 180, 52–58.

Kind, R., Yuan, X.H., 2010. Seismic images of the biggest crash on Earth. Science 329, 1479–1480.

Kind, R., Yuan, X.H., Saul, J., Nelson, D., Sobolev, S.V., Mechie, J., Zhao, W., Kosarev, G., Ni, J., Achauer, U., Jiang, M., 2002. Seismic images of crust and upper mantle beneath Tibet: evidence for Eurasian plate subduction. Science 298 (5596), 1219–1221.

Kneller, E.A., van Keken, P.E., 2007. Trench parallel flow and seismic anisotropy in the Marianas and Andean subduction systems. Nature 450, 1222–1225.

Kosarev, G., Kind, R., Sovolev, S.V., Yuan, X., Hanka, W., Oreshin, S., 1999. Seismic evidence for a detached Indian lithospheric mantle beneath Tibet. Science 283, 1306–1309.

Kreemer, C., Holt, W.E., Haines, A.J., 2003. An integrated global model of present-day motions and plate boundary deformation. Geophys. J. Int. 154, 8–34.

Kumar, M.R., Singh, A., 2008. Evidence for plate motion related strain in the Indian shield from shear wave splitting measurements. J. Geophys. Res. 113, B08306. http://dx.doi.org/10.1029/2007JB005128.

Kumar, P., Yuan, X.H., Kind, R., Ni, J., 2006. Imaging the colliding Indian and Asian lithospheric plates beneath Tibet. J. Geophys. Res. 111, B06308.

Kumar, N., Kumar, M.R., Singh, A., Raju, P.S., Rao, N.P., 2010. Shear wave anisotropy of the Godavari rift in the south Indian shield: rift signature of APM related strain? Phys. Earth Planet. Inter. 181, 82–87.

Lavé, J., Avouac, J.P., Lacassin, R., Tapponnier, P., Montagner, J.P., 1996. Seismic anisotropy beneath Tibet: evidence for eastward extrusion of the Tibetan lithosphere? Earth Planet. Sci. Lett. 140, 83–96.

Lei, J.S., Zhao, D.P., Su, Y.J., 2009. Insight into the origin of the Tengchong intraplate volcano and seismotectonics in southwest China from local and teleseismic data. J. Geophys. Res. 114, B05302. http://dx.doi.org/10.1029/2008JB005881.

Li, C., van der Hilst, R.D., Meltzer, A.S., Engdahl, E.R., 2008. Subduction of the Indian lithosphere beneath the Tibetan Plateau and Burma. Earth Planet. Sci. Lett. 274, 157–168.

Li, Y.H., Wu, Q.J., Pan, J.T., Zhang, F.X., Yu, D.X., 2013. An upper-mantle S-wave velocity model for East Asia from Rayleigh wave tomography. Earth Planet. Sci. Lett. 377–378, 367–377.

Liang, X.F., Shen, Y., Chen, Y.J., Ren, Y., 2011. Crustal and mantle velocity models of southern Tibet from finite frequency tomography. J. Geophys. Res. 116, B02408. http://dx.doi.org/10.1029/2009JB007159.

Liang, X.F., Sandvol, E., Chen, Y.J., Hearn, T., Ni, J., Klemperer, S., Shen, Y., Tilmann, F., 2012. A complex Tibetan upper mantle: a fragmented Indian slab and no southverging subduction of Eurasian lithosphere. Earth Planet. Sci. Lett. 333–334, 101–111.

Liu, K.H., Gao, S.S., 2011. Estimation of the depth of anisotropy using spatial coherency of shear-wave splitting parameters. Bull. Seismol. Soc. Am. 101 (5), 2153–2161.

Lou, X.T., van der Lee, S., Lloyd, S., 2013. AIMBAT: a Python/Matplotlib tool for measuring teleseismic arrival times. Seismol. Res. Lett. 84 (1), 85–93.

Mahéo, G., Guillot, S., Blichert-Toft, J., Rolland, Y., Pêcher, A., 2002. A slab breakoff model for the Neogene thermal evolution of South Karakorum and South Tibet. Earth Planet. Sci. Lett. 195, 45–58.

McNamara, D.E., Owens, T.J., 1994. Shear wave anisotropy beneath the Tibetan Plateau. J. Geophys. Res. 99 (B7), 13655–13665.

Meissner, R., Moonery, W.D., Artemieva, I., 2002. Seismic anisotropy and mantle creep in young orogens. Geophys. J. Int. 149, 1–14.

Müller, R.D., 2007. An Indian cheetah. Nature 449, 795–796.

Nabelek, J., et al., Hi-CLIMB Team, 2009. Underplating in the Himalaya–Tibet collision zone revealed by the Hi-CLIMB experiment. Science 325, 1371–1374.

Özalaybey, S., Chen, W.P., 1999. Frequency-dependent analysis of SKS/SKKS waveforms observed in Australia: evidence for null birefringence. Phys. Earth Planet. Inter. 114, 197–210.

Priestley, K., Debayle, E., McKenzie, D., Pilidou, S., 2006. Upper mantle structure of eastern Asia from multimode surface waveform tomography. J. Geophys. Res. 111, B10304. http://dx.doi.org/10.1029/2005JB004082.

Rosenbaum, G., Gasparon, M., Lucente, F.P., Peccerillo, A., Miller, M.S., 2008. Kinematics of slab tear faults during subduction segmentation and implications for Italian magmatism. Tectonics 27, TC2008. http://dx.doi.org/10.1029/2007TC002143.

Saikia, D., Kumar, M.R., Singh, A., Mohan, G., Dattatrayam, R.S., 2010. Seismic anisotropy beneath the Indian continent from splitting of direct S waves. J. Geophys. Res. 115, B12315. http://dx.doi.org/10.1029/2009JB007009.

Sandvol, E., Ni, J., 1997. Seismic anisotropy beneath the southern Himalayas–Tibet collision zone. J. Geophys. Res. 102 (B8), 17813–17823.

Savage, M.K., 1999. Seismic anisotropy and mantle deformation: what have we learned from shear wave splitting? Rev. Geophys. 37 (1), 65–106.

Silver, P.G., Chan, W.W., 1991. Shear wave splitting and subcontinental mantle deformation. J. Geophys. Res. 96, 16429–16454.

Sol, S., Meltzer, A., Burgmann, R., van der Hilst, R.D., King, R., Chen, Z., Koons, P.O., Lev, E., Liu, Y.P., Zeitler, P.K., Zhang, X., Zhang, J., Zurek, B., 2007. Geodynamics of the southeastern Tibetan Plateau from seismic anisotropy and geodesy. Geology 35 (6), 563–566.

Styron, R., Taylor, M., Okoronkwo, K., 2010. Database of active structures from the Indo-Asian collision. Trans. Am. Geophys. Union 91, 181–182.

Tilmann, F., Ni, J., INDEPTH Seismic Team, 2003. Seismic imaging of the downwelling Indian lithosphere beneath central Tibet. Science 300, 1424–1427.

van Hunen, J., Allen, M.B., 2011. Continental collision and slab break-off: a comparison of 3-D numerical models with observations. Earth Planet. Sci. Lett. 302, 27–37.

VanDecar, J.C., Crosson, R.S., 1990. Determination of teleseismic relative phase arrival times using multi-channel cross-correlation and least squares. Bull. Seismol. Soc. Am. 80, 150–169.

Wang, C.Y., Flesch, L.M., Silver, P.G., Chang, L.J., Chan, W.W., 2008. Evidence for mechanically coupled lithosphere in central Asia and resulting implications. Geology 36 (5), 363–366.

Wessel, P., Smith, W.H.F., 1998. New, improved version of the Generic Mapping Tools released. Trans. Am. Geophys. Union 79, 579.

Wüstefeld, A., Bokelmann, G., Barruol, G.H.R., Zaroli, C., 2008. SplitLab: a shear-wave splitting environment in Matlab. Comput. Geosci. 34, 515–528.

Wüstefeld, A., Bokelmann, G., Barruol, G.H.R., Barruol, G., Montagner, J.-P., 2009. Identifying global seismic anisotropy patterns by correlating shear-wave splitting and surface waves data. Phys. Earth Planet. Inter. 176 (3–4), 198–212.

Xiao, L., Wang, C.Z., Pirajno, F., 2007. Is the underthrust India lithosphere split beneath the Tibetan Plateau? Int. Geol. Rev. 49, 90–98.

Yin, A., 2000. Mode of Cenozoic east–west extension in Tibet suggesting a common origin of rifts in Asia during the Indo-Asian collision. J. Geophys. Res. 105 (B9), 21745–21759.

Yin, A., 2010. Cenozoic tectonic evolution of Asia: a preliminary synthesis. Tectonophysics 488, 293–325.

Yin, A., Harrison, T.M., 2000. Geologic evolution of the Himalayan–Tibetan orogen. Annu. Rev. Earth Planet. Sci. 28, 211–280.

Yuan, X.H., Ni, J., Kind, R., Mechie, J., Sandvol, E., 1997. Lithospheric and upper mantle structure of southern Tibet from a seismological passive source experiment. J. Geophys. Res. 102, 27491–27500.

Zhang, P.Z., Shen, Z.K., Wang, M., Gan, W.J., Burgmaan, R., Monlnar, P., Wang, Q., Niu, Z.J., Sun, J.Z., Wu, J.C., Sun, H.R., You, X.Z., 2004. Continuous deformation of the Tibetan Plateau from global positioning system data. Geology 32 (9), 809–812.

Zhang, Z.J., Chen, Y., Yuan, X.H., Tian, X.B., Klemperer, S.L., Xu, T., Bai, Z.M., Zhang, H.S., Wu, J., Teng, J.W., 2013. Normal faulting from simple shear rifting in South Tibet, using evidence from passive seismic profiling across the Yadong–Gulu Rift. Tectonophysics 606, 178–186.

Zhao, W.J., Nelson, K.D., Project INDEPTH Team, 1993. Deep seismic–reflection evidence for continental underthrusting beneath southern Tibet. Nature 366, 557–559.

Zhao, J.M., Yuan, X.H., Liu, H.B., Kumar, P., Pei, S.P., Kind, R., Zhang, Z.J., Teng, J.W., Ding, L., Gao, X., Xu, Q., Wang, W., 2010. The boundary between the Indian and Asian tectonic plates below Tibet. Proc. Natl. Acad. Sci. USA 107 (25), 11229–11233.

Zhao, W.J., Kumar, P., Mechie, J., Kind, R., Meissner, R., Wu, Z.H., Shi, D.N., Su, H.P., Xue, G.Q., Karplus, M., Tilmann, F., 2011. Tibetan plate overriding the Asian plate in central and northern Tibet. Nat. Geosci. 4, 870–873.

Zhao, J.M., Zhao, D.P., Zhang, H., Liu, H.B., Huang, Y., Cheng, H.G., Wang, W., 2013. P-wave tomography and dynamics of the crust and upper mantle beneath western Tibet. Gondwana Res. 25 (4), 1690–1699.

Zhao, J.M., Murodov, D., Huang, Y., Sun, Y.S., Pei, S.P., Liu, H.B., Zhang, H., Fu, Y.Y., Wang, W., Cheng, H.G., Tang, W., 2014. Upper mantle deformation beneath central–southern Tibet revealed by shear wave splitting measurements. Tectonophysics 627, 135–140.

Zhou, H.W., Murphy, M.A., 2005. Tomographic evidence for wholesale underthrusting of Indian beneath the entire Tibetan plateau. J. Asian Earth Sci. 25, 445–457.